

1 **Experimentally Determined Effects of Olivine Crystallization and Melt Titanium Content**  
2 **on Iron Isotopic Fractionation in Planetary Basalts**

3

4 Kelsey B. Prissel <sup>a</sup>, Michael J. Krawczynski <sup>a</sup>, Nicole X. Nie <sup>b</sup>, Nicolas Dauphas <sup>b</sup>, Hélène Couvy  
5 <sup>a</sup>, Michael Y. Hu <sup>c</sup>, E. Ercan Alp <sup>c</sup>, Mathieu Roskosz <sup>d</sup>

6

7 <sup>a</sup> McDonnell Center for the Space Sciences and Department of Earth and Planetary Sciences,  
8 Washington University in St. Louis, 1 Brookings Drive, St. Louis, MO 63123.

9 <sup>b</sup> Origins Laboratory, Department of the Geophysical Sciences and Enrico Fermi Institute, The  
10 University of Chicago, 5734 South Ellis Avenue, Chicago, IL 60637.

11 <sup>c</sup> Advanced Photon Source, Argonne National Laboratory, 9700 South Cass Avenue, Argonne, IL  
12 60439

13 <sup>d</sup> IMPMC, CNRS UMR 7590, Sorbonne Universités, Université Pierre et Marie Curie, IRD,  
14 Muséum National d'Histoire Naturelle, CP 52, 57 rue Cuvier, Paris F-75231, France

15

16

17 Corresponding author: Kelsey B. Prissel, [k.b.williams@wustl.edu](mailto:k.b.williams@wustl.edu)

18

19

20 Abstract

21 Olivine is the most abundant mantle mineral at depths relevant to oceanic crust production  
22 through melting. It is also a liquidus phase for a wide range of mafic and ultramafic magma  
23 compositions. We have experimentally investigated the effects of olivine crystallization and melt  
24 composition on the fractionation of Fe isotopes in igneous systems. To test whether there is a melt  
25 compositional control on Fe isotopic fractionation, we have conducted nuclear resonant inelastic  
26 X-ray scattering (NRIXS) measurements on a suite of synthetic glasses ranging from 0.4 to 16.3  
27 wt.%  $\text{TiO}_2$ . The resulting force constants are similar to those of the reduced ( $f\text{O}_2 = \text{IW}$ ) terrestrial  
28 basalt, andesite, and dacite glasses reported by Dauphas et al. (2014), indicating that there is no  
29 measurable effect of titanium composition on Fe isotopic fractionation in the investigated  
30 compositional range. We have also conducted olivine crystallization experiments and analyzed the  
31 Fe isotopic composition of the experimental olivines and glasses using solution MC-ICPMS.  
32 Olivine and glass separates from a given experimental charge have the same iron isotopic  
33 composition within error. This result is robust in both the high-Ti glass (Apollo 14 black) and low-  
34 Ti glass (Apollo 14 VLT) compositions, and at the two oxygen fugacities investigated (IW-1,  
35 IW+2). Additionally, we have determined that Fe loss in reducing one-atmosphere gas-mixing  
36 experiments occurs not only as loss to the Re wire container, but also as evaporative loss, and each  
37 mechanism of experimental Fe loss has an associated Fe isotopic fractionation.

38 We apply our results to interpreting Fe isotopic variations in the lunar mare basalts and  
39 lunar dunite 72415-8. Our experimental results indicate that neither melt  $\text{TiO}_2$  composition nor  
40 equilibrium olivine crystallization can explain the observed difference in the iron isotopic  
41 composition of the lunar mare basalts. Additionally, equilibrium iron isotopic fractionation  
42 between olivine and melt cannot account for the “light” iron isotopic composition of lunar dunite

43 72415-8, unless the melt from which it is crystallizing was already enriched in light iron isotopes.  
44 Our results support models of diffusive fractionation to explain the light iron isotopic compositions  
45 measured in olivine from a variety of rock types and reduced ( $fO_2 = IW-1$  to  $IW+2$ ) igneous  
46 environments (e.g., lunar dunite and basalts, terrestrial peridotites and basalts, martian  
47 shergottites).

48

## 49 **1. Introduction**

50 Analytical developments over the past decade have revealed that igneous rocks and  
51 minerals display variations in the isotopic composition of non-traditional stable isotope systems  
52 (i.e., not C, H, N, O, S Teng et al., 2017, and references therein). The degree of mass-dependent  
53 fractionation between stable isotopes has been attributed to factors such as oxidation state, bonding  
54 environment, and volatility. While early studies focused on low-temperature stable isotopic  
55 fractionation, a growing number of studies have revealed measurable isotopic fractionations  
56 present in high temperature igneous systems (e.g., Beard and Johnson, 2004; Poitrasson et al.,  
57 2004; Weyer et al., 2005; Williams et al., 2005; Teng et al., 2008, and subsequent studies).  
58 Interpretations of these variations are often hampered by the paucity of equilibrium fractionation  
59 factors between coexisting phases, which limits quantitative modeling of the relevant igneous  
60 processes.

61 High-temperature stable isotopic fractionations have been used to elucidate planetary-scale  
62 processes, such as the formation of the Moon, as well as smaller scale processes, such as the  
63 differentiation of magma. In particular, high-precision studies of stable isotopes have resolved  
64 isotopic differences between terrestrial and lunar samples for certain elements (e.g., Wang and  
65 Jacobsen, 2016). However, for many isotopic systems, it is difficult to tell whether the Earth and

66 Moon have different isotopic compositions because the processes of magmatic differentiation,  
67 including lunar magma ocean crystallization and later magma generation and crystallization, have  
68 imparted stable isotopic variations to lunar rocks that need to be understood and disentangled  
69 before a claim can be made regarding the bulk composition of the Earth or Moon. The increased  
70 precision of modern isotope analyses has resolved a “dichotomy” present between the bulk stable  
71 isotopic compositions of the low-Ti and high-Ti mare basalts on the Moon (Figure 1). Specifically,  
72 this dichotomy has been observed for Fe (Wiesli et al., 2003; Poitrasson et al., 2004; Weyer et al.,  
73 2005; Craddock et al., 2010; Liu et al., 2010; Sossi and Moynier, 2017), with high-Ti mare basalts  
74 being isotopically “heavy” compared to low-Ti basalts ( $\delta^{56}\text{Fe}_{\text{high-Ti}} > \delta^{56}\text{Fe}_{\text{low-Ti}}$ ). The dichotomy  
75 was also observed for Mg ( $\delta^{26}\text{Mg}_{\text{high-Ti}} < \delta^{26}\text{Mg}_{\text{low-Ti}}$ ; Sedaghatpour et al., 2013), Li ( $\delta^7\text{Li}_{\text{high-Ti}} >$   
76  $\delta^7\text{Li}_{\text{low-Ti}}$ ; Day et al., 2016), and Ti ( $\delta^{49}\text{Ti}_{\text{high-Ti}} > \delta^{49}\text{Ti}_{\text{low-Ti}}$ ; Millet et al., 2016). Though the  
77 difference in stable isotopic compositions between the high- and low-Ti basalts is well documented  
78 analytically, the petrologic processes responsible for the lunar isotopic dichotomy remain elusive.

79 Despite increasing evidence for high-temperature isotopic fractionation in igneous rocks  
80 (e.g., Dauphas and Rouxel, 2006; Dauphas et al., 2017), there is a paucity of experimental studies  
81 of isotopic fractionation during magmatic differentiation of mafic compositions. The iron isotopic  
82 compositions of igneous rocks have been extensively studied, and the documented isotopic  
83 variations in igneous rocks are caused by a combination of partial melting (e.g., Williams et al.,  
84 2005; Weyer and Ionov, 2007; Dauphas et al., 2009a; Dauphas et al., 2014; Williams and Bizimis,  
85 2014), equilibrium and fractional crystallization (e.g., Teng et al., 2008; Dauphas et al., 2014;  
86 Roskosz et al., 2015), and diffusive fractionation (e.g., Dauphas and Rouxel, 2006; Sio et al., 2013;  
87 Oeser et al., 2015; Sio and Dauphas, 2016; Collinet et al., 2017). Experimental studies of  
88 equilibrium Fe isotope partitioning at high temperature have investigated metal-silicate systems,

89 fayalite-magnetite fractionation, as well as Fe isotopic fractionation between evolved rhyolitic  
90 compositions and sulfides (e.g., Schuessler et al., 2007; Shahar et al., 2008; Poitrasson et al., 2009).  
91 Additionally, Dauphas et al. (2014) investigated the Fe bonding structure in a suite of terrestrial  
92 volcanic glass compositions ranging from basalt to rhyolite, concluding that Fe isotopic  
93 composition is influenced by the redox state of iron and the silica content of the melt.

94 Evidence for mineralogical, compositional, and redox controls on Fe isotope partitioning  
95 in igneous rocks highlights the importance of experimentally quantifying mineral-melt  
96 fractionations for major rock-forming minerals. Olivine is a ubiquitous mineral on rocky,  
97 differentiated planetary bodies. Even a small ( $<0.1\text{\textperthousand}$ ) olivine-melt Fe isotopic fractionation could  
98 significantly fractionate the Fe isotopes in mantle reservoirs during planetary differentiation; for  
99 example, an olivine-melt fractionation  $\delta^{56}\text{Fe}_{\text{olivine}} - \delta^{56}\text{Fe}_{\text{melt}} = -0.05\text{\textperthousand}$  would increase the  $\delta^{56}\text{Fe}$  of  
100 a magma ocean by  $0.1\text{\textperthousand}$  after 50% fractional crystallization of olivine. The measured iron isotopic  
101 compositions of olivine separates are often used to interpret olivine-melt fractionations (e.g.,  
102 Williams et al., 2005; Wang et al., 2015). Yet, naturally occurring minerals have complex  
103 crystallization-cooling histories, and inferring an equilibrium fractionation factor from such  
104 measurements is fraught with difficulties. The use of natural samples to determine olivine-melt  
105 equilibrium iron isotopic fractionations is complicated by diffusion-driven, kinetic iron isotopic  
106 fractionations (e.g., Teng et al., 2008; Teng et al., 2011; Sio et al., 2013). In terrestrial igneous  
107 rocks, both  $\text{Fe}^{2+}$  and  $\text{Fe}^{3+}$  coexist, which can cause equilibrium isotopic fractionation between melt  
108 and olivine (i.e., Teng et al., 2008; Dauphas et al., 2009a). Redox-driven fractionation on Earth  
109 may obscure the existence of equilibrium iron isotopic fractionation between olivine and  $\text{Fe}^{2+}$  in  
110 silicate melt. On the other hand, large Fe isotopic fractionations exist among lunar basalts in an  
111 environment relatively free of  $\text{Fe}^{3+}$ . The absence of  $\text{Fe}^{3+}$  on the Moon supports mechanisms of

112 mineral fractionation, melt composition, and/or diffusive re-equilibration as cause for the observed  
113 iron isotopic variation between the low- and high-Ti mare basalts. The iron isotopic fractionations  
114 associated with these equilibrium and kinetic processes need to be well-characterized in order to  
115 distinguish the effects of each process on the resulting iron isotopic compositions of igneous rocks.

116 To investigate the effects of melt composition and olivine crystallization on Fe isotopic  
117 fractionation, we have experimentally determined the olivine-melt equilibrium partitioning of Fe  
118 isotopes for a compositional suite of synthetic lunar volcanic glasses. We have implemented a dual  
119 approach, combining independent techniques (MC-ICPMS and NRIXS) for determining  
120 equilibrium Fe isotopic fractionations between high temperature phases. In focusing our  
121 experimental study on compositions and oxygen fugacities relevant for lunar differentiation, we  
122 investigated Fe isotopic fractionation in the case where  $\text{Fe}^{3+}$  is of negligible abundance.  
123 Furthermore, in experimentally examining the Fe isotope dichotomy between high-Ti and low-Ti  
124 lunar mare basalts, we have examined whether the bulk titanium content of a melt exhibits a  
125 compositional control on the resulting Fe isotope signature of the basalt.

126

## 127 2. Methods

128 We have investigated the equilibrium fractionation of Fe isotopes between olivine and melt  
129 using two independent techniques. To determine the melt compositional control on Fe isotopic  
130 fractionation between lunar melts and olivine, we have conducted nuclear resonant inelastic X-ray  
131 scattering (NRIXS) measurements on a suite of synthetic glasses ranging from 0.4 to 16.3 wt.%  
132  $\text{TiO}_2$ . To evaluate the magnitude of iron isotopic fractionation at equilibrium between olivine and  
133 melt, we have conducted olivine crystallization experiments and analyzed the Fe isotopic  
134 composition of the experimental olivines and glasses using solution MC-ICPMS. Direct olivine

135 crystallization experiments were conducted using two bulk compositions: a synthetic glass similar  
136 to Apollo 14 VLT (very low Ti), and a synthetic Apollo 14 black glass (Table 1). Both of these  
137 compositions have olivine as a liquidus phase at one atmosphere pressure.

138 In comparing the results of both the NRIXS and direct crystallization experimental  
139 methods, we have determined the effect of equilibrium olivine crystallization and melt titanium  
140 content on Fe isotopic fractionation during high-temperature igneous processes. Additionally, the  
141 reducing experimental run conditions minimize  $\text{Fe}^{3+}$  content in the olivine and glass, making our  
142 results directly applicable to lunar oxygen fugacity conditions (IW-2 to IW+1; Sato, 1973).

143

#### 144 2.1. Starting materials

145 For the NRIXS measurements, synthetic lunar ultramafic volcanic glass compositions were  
146 prepared from oxide powders to match the Apollo 16 green (0.39 wt.%  $\text{TiO}_2$ ), Apollo 14 yellow  
147 (4.58 wt.%  $\text{TiO}_2$ ), Apollo 17 orange (8.63 wt.%  $\text{TiO}_2$ ), and Apollo 14 black (16.4 wt.%  $\text{TiO}_2$ ) glass  
148 compositions given in Delano (1986) (Table 1). These glasses were chosen to span the range of  
149  $\text{TiO}_2$  content in the picritic lunar glass suite. Sodium and potassium were added to the mixtures as  
150 carbonates ( $\text{Na}_2\text{CO}_3$ ,  $\text{K}_2\text{CO}_3$ ), calcium was added as  $\text{CaSiO}_3$ , and all other components were added  
151 as single element oxides. In order to perform the NRIXS measurements, which are only sensitive  
152 to the Mössbauer isotope  $^{57}\text{Fe}$ ,  $^{57}\text{Fe}$ -enriched  $\text{Fe}_2\text{O}_3$  powder (96.64%  $^{57}\text{Fe}$ , Cambridge Isotopes)  
153 was used. Oxides were mixed by hand under isopropanol in an agate mortar and pestle for 20  
154 minutes.

155 For the olivine crystallization experiments, the starting materials were prepared to be  
156 similar in composition to the synthetic Apollo 14 VLT (green) and Apollo 14 black glasses in  
157 Delano (1986) (Table 1). Calcium was added as  $\text{CaCO}_3$  for the green glass, and  $\text{CaTiO}_3$  for the

158 black glass. Compositions used for the olivine crystallization experiments contained natural Fe  
159 isotope abundances and were mixed without the addition of Cr, Na, or K. Oxides, silicates,  
160 carbonates, and titanates were mixed under isopropanol in a silicon-nitride ball mill for 3 hours.  
161 Polyvinyl alcohol was added as a binding agent to the starting material mixtures for both the  
162 NRIXS and olivine crystallization techniques. Once dry, 75 mg aliquots of each mixture were  
163 pressed into cylindrical pellets of 4 mm diameter and 2 mm height in preparation to be melted in  
164 the gas-mixing furnace. Great care was exercised to ensure that no cross-contamination took place  
165 between the experiments involving enrichment in  $^{57}\text{Fe}$  and those with natural Fe isotopic  
166 abundances. However, select experiments did exhibit slight enrichments in  $^{57}\text{Fe}$  (as detailed in the  
167 Supplementary Material). By focusing on  $\delta^{56}\text{Fe}$ , we minimize any potential effects of  $^{57}\text{Fe}$   
168 contamination.

169

## 170 2.2. Experimental Methods

171 Lunar volcanic glass syntheses and olivine crystallization experiments were conducted in  
172 vertical gas-mixing furnaces at Washington University in St. Louis. Sample pellets were fused to  
173 rhenium loops and hung by a Pt wire thread in the furnace hot spot for the run duration.  
174 Experimental samples were then quenched rapidly by melting the Pt hanging wire and dropping  
175 the sample from within the furnace into a beaker of deionized water. The  $^{57}\text{Fe}$ -doped glass  
176 syntheses were conducted for approximately 3 hours at 1400°C and an oxygen fugacity  
177 corresponding to the iron-wüstite buffer (Table 2). Olivine crystallization experiments were  
178 conducted at  $f\text{O}_2$  values of IW-1 and IW+2 for durations of 6 hours, 1 day, and 4 days (Table 2).  
179 The temperatures for the olivine crystallization experiments ranged from 1262 to 1269°C, with

180  $\pm 1^{\circ}\text{C}$  variation during a given experimental run (Table 2). These temperatures were optimal for  
181 producing low modal abundances (10-20 wt.%) of large olivine crystals.

182 All experimental run products were synthesized at oxygen fugacities that bracket the  
183 oxygen conditions inferred for the Moon. These reducing conditions minimize the presence of  
184  $\text{Fe}^{3+}$ , which has been demonstrated to affect Fe isotope partitioning (e.g., Dauphas et al., 2014). A  
185 controlled flow of  $\text{H}_2$  and  $\text{CO}_2$  gases buffered the oxygen fugacity throughout each experiment.  
186 The fugacity was monitored with a Ca-doped zirconia oxygen probe using air as the reference gas.  
187 The  $f\text{O}_2$  was found to vary between 0.01 to 0.15 log units ( $1\sigma$  standard deviation) during a given  
188 experiment (Table 2).

189 Long experimental run durations aided in crystal growth, allowing for clean mechanical  
190 separation of olivine grains for MC-ICPMS work. Olivine grains from our four-day experiments  
191 exhibited a range in grain diameter from 20 to 100  $\mu\text{m}$ , compared to the 5 to 50  $\mu\text{m}$  grain diameter  
192 range for the one-day experiments (Figure 2). However, Fe loss from an experimental charge  
193 increases with increased run duration (Table 2, Figure 3a). Thus, a four-day run duration was  
194 deemed optimal for the olivine crystallization experiments needed to minimize Fe loss from the  
195 experiment, while providing experimental olivines large enough to hand-separate for MC-ICPMS  
196 measurements. To ensure that clean olivine and glass could be retrieved for MC-ICPMS work,  
197 olivine and glass were separated from the four-day experiments. Quantitative analysis of the Fe  
198 loss in these experiments is presented in Section 4.1.

199

200 2.3. Approach to equilibrium

201 The experimentally produced olivines are compositionally homogenous and do not exhibit  
202 compositional zoning within the grains (Figure 2), and electron microprobe compositional

203 analyses show low standard deviations amongst all analyzed grains in a given sample (Table 3).  
204 Mineral-liquid Fe-Mg exchange coefficients ( $K_D^{Fe-Mg}$ , Table 2) for our olivine-bearing experiments  
205 are a function of melt Ti content (0.32-0.34 for 0.06 wt.%  $TiO_2$ ; 0.23-0.26 for 18 wt.%  $TiO_2$ ) and  
206 are consistent with the results of Krawczynski and Grove (2012). In addition, a time series of  
207 experiments was conducted for each experimental starting composition (Apollo 14 VLT green  
208 glass, Apollo 14 black glass) at each experimental oxygen fugacity (IW-1, IW+2) in order to  
209 evaluate the effect of experimental Fe loss on the olivine-melt equilibrium. Experimental iron loss  
210 increases with increased run duration and decreased oxygen fugacity (Table 2). Thus, the lowest  
211 oxygen fugacity ( $fO_2 = IW-1$ ) experiments experienced significant (up to 18%) Fe loss during the  
212 four-day experiments (see discussion in Section 4.1). Despite the increased Fe loss, the mineral-  
213 liquid Fe-Mg exchange coefficients for the four-day experiments are the same as those calculated  
214 for the shorter duration experiments (Table 2), indicating that olivine-melt equilibrium was  
215 maintained.

216

#### 217 2.4. Analytical Methods

##### 218 2.4.1. Electron Microprobe Analysis

219 Experimental run products were analyzed for major element abundances using the JEOL  
220 JXA-8200 electron microprobe at Washington University in St. Louis. Standardization was  
221 performed with a beam diameter of 20  $\mu m$  on natural and synthetic glass and mineral samples. We  
222 used the mean atomic number (MAN) method (Donovan et al., 2016) for wavelength dispersive  
223 spectrometer background correction and measured the following elements: Si, Al, Ti, Cr, Fe, Mn,  
224 Mg, Ca, Na, K. Each quantitative analysis used a 15 kV accelerating potential and 25 nA beam  
225 current. Glass compositions were analyzed with a 20  $\mu m$  beam diameter, and olivine compositions

226 were analyzed with a focused beam ( $\sim 1 \mu\text{m}$  diameter). Each compositional data point was reduced  
227 using *Probe for EPMA* software. Averages of the analyzed glass and olivine compositions are  
228 reported in Table 3. Only analyses with totals 98.5-101.5 weight percent (wt.%) are included in  
229 the reported averages (with the exception of experiment J021, for which the analytical totals were  
230 on average 96.75 wt.% likely due to incomplete degassing of the carbonates in the starting  
231 material). Olivine analyses were filtered to include only those with olivine stoichiometry (cation  
232 total between 2.98-3.02 for 4 oxygen atoms). The same calibration was used for the compositional  
233 analysis of the experimental wires, with pure Re, Fe, and Pt metal samples added as analytical  
234 standards. The Re experiment wires were analyzed from core to rim with a  $2 \mu\text{m}$  beam diameter.

235

236 2.4.2. Nuclear Resonant Inelastic X-ray Scattering Spectroscopy (NRIXS) Methods

237 Nuclear resonant inelastic X-ray scattering spectroscopy (NRIXS) was used to probe the  
238 excitation modes of iron atoms and derive quantities needed to calculate equilibrium fractionation  
239 factors. From the phonon excitation probability function,  $S(E)$ , or the partial phonon density of  
240 states,  $g(E)$ , (itself derived from  $S$ ), the force constant for the iron sublattice can be extracted (e.g.,  
241 Dauphas et al., 2012; Dauphas et al., 2014; Liu et al., 2017) (also see Polyakov et al., 2007 for a  
242 different approach based on the kinetic energy). Assuming that the bonds are harmonic and given  
243 the high temperatures involved in magmatic processes, the reduced partition function ratio, or  $\beta$ -  
244 factor is calculated as a function of temperature from the mean force constant of the iron bonds,  
245  $\langle F \rangle$  in N/m (the higher order terms needed to calculate iron  $\beta$ -factors at low temperature are given  
246 in Table 4):

$$247 \quad 1000 \ln \beta = 2904 \frac{\langle F \rangle}{T^2} \quad (1)$$

249 At a given temperature, the equilibrium stable isotopic fractionation factor (e.g.,  $\alpha_{\text{mineral}}$ -  
250  $_{\text{melt}}$ ) between two phases is related to the  $\beta$ -factor and Fe isotopic composition ( $\delta^{56}\text{Fe}$ ) for each  
251 phase through:

252

253  $1000 \ln \alpha_{\text{mineral-melt}} = \delta^{56}\text{Fe}_{\text{mineral}} - \delta^{56}\text{Fe}_{\text{melt}} = 1000 \ln \beta_{\text{mineral}} - 1000 \ln \beta_{\text{melt}}$   
254 (2)

255 Using the measured force constants for synthetic lunar glasses and olivine (Dauphas et al., 2014),  
256 the equilibrium fractionation factor between olivine and melt can be theoretically determined using  
257 equation (2), assuming that the iron force constant in the glass is not significantly different from  
258 that of a melt of the same composition.

259

260 2.4.3. Multicollector-Inductively Coupled Plasma Mass Spectrometry (MC-ICPMS) Methods

261 The quenched experimental samples were crushed, and then individual phases were hand  
262 separated for Fe isotopic analysis with a Thermo Scientific Neptune MC-ICPMS in the Origins  
263 Lab at the University of Chicago. The instrument was upgraded in the course of its life by addition  
264 of an OnToolBooster Jet pump, bringing it to specifications on par with the Neptune Plus model.  
265 Olivine grains were hand-picked from the experimental samples under an optical microscope using  
266 cross-polarized light to distinguish the birefringent olivines from the isotropic glass. Separated  
267 olivine grains ranged between 30 and 100  $\mu\text{m}$  in diameter and contained minor amounts of glass,  
268 present as thin layers on the edge of the grains. Glass separates were approximately 50-150  $\mu\text{m}$  in  
269 diameter, and the transparency of the glass allowed for separation of glass pieces that were free of  
270 olivine grains.

271 Olivine and glass separates were then dissolved for MC-ICPMS analysis. The starting  
272 material powders, used experiment wires, and “total samples” (experimental sample left after  
273 minor glass and olivine separate removal) were also dissolved and measured to aid in interpretation  
274 of the measured isotopic compositions (see Section 4.1). Following the routine sample dissolution  
275 protocol of the Origins Lab (e.g., Dauphas et al., 2009b; Craddock and Dauphas, 2011), we  
276 digested 10-40 mg of each sample through hot-plate acid dissolution with mixtures of concentrated  
277 HF-HNO<sub>3</sub>-HClO<sub>4</sub> and HCl-HNO<sub>3</sub>-HClO<sub>4</sub>. An additional dissolution step using aqua regia (3:1  
278 ratio of HCl-HNO<sub>3</sub>) was used for the starting material powders, Re wires, and “total samples”.  
279 This step was repeated three times to ensure all of the Fe had been dissolved from the samples.  
280 However, a white residue (rich in TiO<sub>2</sub> and Al<sub>2</sub>O<sub>3</sub>), remained after two weeks of dissolution for  
281 the starting material powders and “total samples”. Analysis of the white residues by electron  
282 dispersive spectroscopy confirmed that there was no Fe present, indicating that the dissolution  
283 effectively removed all Fe from the samples despite the remaining white residue. After the heated  
284 dissolution steps, each sample was dried out (the samples with visible residues were centrifugated  
285 and the supernatants were used), then dissolved in 6M HCl in preparation for Fe column chemistry.

286 The sample solutions were purified for Fe through column chemistry following the routine  
287 methods of the Origins Lab at the University of Chicago (e.g., Dauphas et al., 2004; Dauphas and  
288 Rouxel, 2006; Dauphas et al., 2009b). The iron isotopic compositions of the sample solutions were  
289 measured using the standard-bracketing method of Dauphas et al. (2009b), and are reported as  
290  $\delta^{56}\text{Fe}$  relative to IRMM-524, whose isotopic composition is identical to IRMM-014 (Craddock  
291 and Dauphas, 2011).

292

293 3. Results

294        Here we report experimentally determined mean force constants of iron bonds in synthetic  
295    glass samples and iron isotopic compositions of synthetic olivine and glass separates. Iron isotopic  
296    fractionation factors determined from the force constants and iron isotopic compositions  
297    demonstrate an absence of resolvable iron isotopic fractionation during olivine crystallization in  
298    reducing ( $fO_2 = IW-1$  to  $IW+2$ ) conditions.

299

### 300    3.1. NRIXS Results

301        The force constants calculated from NRIXS spectra on our synthetic lunar glasses show  
302    that within error, the lunar glasses have the same force constant, averaging to a value of  $195 \pm 22$   
303    N/m (Table 4). This similarity in force constants over the 0.4 – 16.3 wt.%  $TiO_2$  range of our  
304    synthetic glasses suggests that Fe isotopic fractionation is not a function of melt Ti content (Figure  
305    4). Further, the mean force constants of our synthetic suite of lunar glasses are similar to the force  
306    constants generated for reduced ( $fO_2 = IW$ ) terrestrial basalts ( $197 \pm 8$  N/m) in Dauphas et al.  
307    (2014). The force constants from the synthetic lunar glasses are also similar to the previously  
308    determined iron force constant for olivine ( $Fe_{86}$ ,  $Fe^{3+}$  absent) of  $197 \pm 10$  N/m (Dauphas et al.,  
309    2014).

310

### 311    3.2. Olivine Crystallization Experiments

312        The measured Fe isotopic compositions of the experimental glass and olivine separates  
313    indicate that there is no measurable fractionation between olivine and glass (Table 5). The isotopic  
314    difference between the starting material, experiment wire, and olivine and glass separates can be  
315    explained by the fractionation of Fe isotopes during experimental Fe loss to the Re wire and  
316    through evaporation (Section 4.1). The iron isotopic composition of the starting material powders

317 (Table 5) is controlled by both the iron isotopic composition of  $\text{Fe}_2\text{O}_3$  (used in all starting  
318 compositions) and Fe metal sponge (used only in starting compositions #010 and #011) (Appendix  
319 Table 1). To further illustrate the isotopic relationship among all experimental parts, the measured  
320 Fe isotopic compositions have been plotted in Figure 5. For each experiment, the olivine Fe  
321 isotopic composition is indistinguishable from that of the glass. The measured compositions thus  
322 indicate that olivine does not significantly fractionate iron isotopes when crystallizing from lunar  
323 melt compositions at lunar-like  $f\text{O}_2$ .

324

325 4. Discussion

326 4.1. Quantitative analysis of experiment iron loss

327 The four-day olivine crystallization experiments experienced up to 18% total Fe loss (Table  
328 2). We estimated the amount of total Fe loss using a mass balance of the measured phase  
329 compositions and the bulk starting composition of the experiment (Krawczynski and Olive, 2011).  
330 A rhenium wire was used in all of the experiments to minimize the diffusive Fe loss to the metal  
331 loop at reduced oxygen fugacities (Borisov and Jones, 1999). The experimental runs at  $f\text{O}_2 = \text{IW} + 2$   
332 experienced less Fe loss than those at  $f\text{O}_2 = \text{IW} - 1$  (9% vs. 18% Fe loss, Table 2). The total amount  
333 of iron lost from our experiments under reducing conditions is consistent with the estimated loss  
334 in experiments ran at similar conditions by Borisov and Jones (1999). Electron microprobe  
335 analyses of the Re wires after completion of the experiments (Figure 3b, Appendix Table 2) yield  
336 Fe concentrations within the range of those measured in Re wires from Borisov and Jones (1999).  
337 The Re wire is always enriched in the light isotopes of iron, which is consistent with the fact that  
338 transport through the wire is diffusive, and light isotopes of iron diffuse faster than heavier ones  
339 (Mullen, 1961; Roskosz et al., 2006; Dauphas, 2007; Richter et al., 2009; Van Orman and

340 Krawczynski, 2015). However, the Fe mass balance between the wire and sample cannot account  
341 for all of the sample Fe loss.

342 To account for the effect of Fe loss on the measured Fe isotopic compositions of the samples,  
343 we measured the Fe isotopic compositions of the bulk starting material, experiment wire, and the  
344 sample material remaining after olivine and glass separates were removed (Table 5). Owing to  
345 their similar Fe isotopic compositions, removal of minor olivine and glass fractions from the  
346 sample did not change the bulk isotopic composition of the remaining sample material (un-  
347 separated glass and olivine, hereafter referred to as “total sample”). For each of the olivine  
348 crystallization experiments, the isotopic compositions ( $\delta^{56}\text{Fe}$ ) of the total sample were higher than  
349 that for the bulk starting material. Open system behavior of Fe and isotopic fractionation between  
350 the bulk starting material and the total sample can be explained by Fe loss to the Re wire and  
351 evaporative Fe loss in the gas-mixing furnace. Using the measured iron isotopic compositions of  
352 the bulk starting material, experiment wire, and the total sample, we were able to quantify the mass  
353 of Fe lost and the associated Fe isotopic fractionation for both mechanisms of Fe loss occurring  
354 during an experimental run.

355 The incorporation of Fe into Re wire during the experiment induced some Fe isotopic  
356 fractionation, with the wire having a lighter iron isotopic composition than the total sample (Table  
357 5, Figure 5). Roskosz et al. (2006) demonstrated that experimental iron loss to Pt wires fractionates  
358 iron isotopes. In that study, kinetic fractionation of Fe isotopes produced an isotopically light Pt  
359 wire (relative to the experimental sample) in short duration experiments. In longer duration  
360 experiments, Fe isotopes equilibrated between the Pt wire and experimental charge producing an  
361 isotopically heavier Pt wire, which presumably represented the equilibrium partitioning of stable  
362 Fe isotopes between Pt and melt. Similar to the Pt wire results of Roskosz et al. (2006), the Re

363 wires from our experiments are isotopically lighter than the experimental samples. This is most  
364 likely associated with diffusive transport of iron, as it is well-documented in a variety of systems  
365 that light isotopes diffuse faster than heavier ones (e.g., Richter et al., 2009; Van Orman and  
366 Krawczynski, 2015), resulting in light isotope enrichment in the reservoir that experiences net Fe  
367 gain (i.e., the Re wire) relative to the source (i.e., the silicate melt). Owing to this kinetic  
368 fractionation, iron isotopes are more fractionated between the Re wire and total sample in the  
369 experiments that experienced less iron loss ( $fO_2 = IW + 2$ ). That is, as more Fe diffuses into the Re  
370 wire, the fractionation between the wire and the sample decreases. Only one sample (H055) has a  
371 Re wire iron isotopic composition that is heavier than the iron isotopic composition of the bulk  
372 starting material, however the wire is still isotopically lighter than the glass. Owing to the presence  
373 of a thin glass coating on the H055 wire, it is possible that a minor amount of experimental glass  
374 was dissolved along with the wire during preparation for iron isotope measurement. This would  
375 result in a measured iron isotopic composition for the wire that is heavier than the iron isotopic  
376 composition of the wire without glass.

377 Although loss of Fe to the Re wire fractionates Fe isotopes and produces a heavier Fe isotopic  
378 composition for the total sample relative to the bulk starting material, the total amount of Fe  
379 incorporated into the wire cannot account for the magnitude of Fe isotopic fractionation between  
380 the two, nor the bulk Fe loss. Similar to Fe loss to the Re wire, evaporative Fe loss would  
381 preferentially deplete the experiments in lighter Fe isotopes, resulting in greater  $\delta^{56}\text{Fe}$  for the  
382 olivine, glass, and total sample compared to the bulk starting material.

383 To assess the extent of both evaporative Fe loss and Fe loss to the Re wire, we calculated an  
384 isotopic mass balance of the measured experiment parts (starting material, wire, and total sample)  
385 and, by difference, the Fe that evaporated during the experiment. For example, using the isotopic

386 measurements (Table 5) for each part of experiment H056 we can estimate a  $\delta^{56}\text{Fe}$  for the Fe lost  
387 by evaporation:

388

389

$$\delta^{56}\text{Fe}_{\text{starting material}} = \sum_i (X_{\text{Fe}}^i \times \delta^{56}\text{Fe}_i) \quad (3)$$

390

391 where  $i$  denotes a reservoir of the experiment (wire, total sample, gas), where  $X_{\text{Fe}}$  represents the  
392 mass fraction of the initial Fe present in each reservoir,  $\delta^{56}\text{Fe}_{\text{starting material}}$ ,  $\delta^{56}\text{Fe}_{\text{total sample}}$ ,  $\delta^{56}\text{Fe}_{\text{wire}}$  are  
393 measured values, and  $\delta^{56}\text{Fe}_{\text{gas}}$ ,  $X_{\text{Fe}}^{\text{wire}}$ ,  $X_{\text{Fe}}^{\text{total sample}}$ ,  $X_{\text{Fe}}^{\text{gas}}$  can then be calculated from mass balance  
394 constraints (results presented in Figure 6).  $X_{\text{Fe}}^{\text{total sample}}$  is equivalent to one minus the percent total  
395 Fe loss estimated from mass balance of the measured phases and the experimental starting  
396 composition (Krawczynski and Olive, 2011). For H056, which experienced 18% total Fe loss,  
397  $X_{\text{Fe}}^{\text{total sample}} = 0.82$  (Figure 6b).  $X_{\text{Fe}}^{\text{wire}}$  is calculated using the ICP-MS Fe concentration measurement  
398 of the dissolved wire ( $\mu\text{g}$ , Table 5) and the estimated mass of Fe in the starting material (75 mg  
399 pellet, wt.% FeO for starting composition, Table 1). For H056,  $X_{\text{Fe}}^{\text{wire}} = 0.04$ . Following this,  $X_{\text{Fe}}^{\text{gas}}$   
400 can be calculated assuming  $X_{\text{Fe}}^{\text{total sample}} + X_{\text{Fe}}^{\text{wire}} + X_{\text{Fe}}^{\text{gas}} = 1$ . Thus, for H056,  $X_{\text{Fe}}^{\text{gas}} = 0.14$ . From this  
401 calculation, we conclude that 14% of the initial Fe in the starting material was lost by evaporation  
402 during the experiment.

403 The last unknown of equation (3) is the “iron isotopic composition” of the Fe lost through  
404 evaporation ( $\delta^{56}\text{Fe}_{\text{gas}}$ ), or rather the net isotopic fractionation that resulted from the evaporation.  
405 To estimate the evaporative fractionation, we solve equation (3) for  $\delta^{56}\text{Fe}_{\text{gas}}$  using the  $X_{\text{Fe}}$  values  
406 calculated above (Figure 6b) and the measured  $\delta^{56}\text{Fe}$  values for the experiment parts (Table 5). For  
407 H056, the resulting isotopic composition associated with the evaporated gas is  $\delta^{56}\text{Fe}_{\text{gas}} = -2.01\text{\textperthousand}$ ,  
408 and the bulk isotopic fractionation factor is  $\alpha_{\text{experiment-vapor}} = 1.0028$ . Our estimates of the evaporative

409 isotopic fractionation based on the mass balance of our measured experimental run products (bulk  
410  $\alpha_{\text{experiment-vapor}}$ ) range from 1.0002 to 1.0028, with the smallest fractionation between experiment and  
411 vapor (1.0002) existing for experiment J012, the high-Ti (black glass) composition conducted at  
412 IW+2. The experiment-vapor fractionation in our gas-mixing furnace experiments is smaller than  
413 that in a vacuum furnace because the Fe vapor pressure is higher, which dampens the isotopic  
414 fractionation (Richter et al., 2002; Richter, 2004; Dauphas and Rouxel, 2006; Richter et al., 2007;  
415 Richter et al., 2009; Dauphas et al., 2015). Most likely, the evaporative Fe loss proceeded through  
416 a Rayleigh distillation. Using the  $\alpha_{\text{experiment-vapor}}$  calculated for each experiment, we have modeled  
417 the change in the iron isotopic composition of the experimental sample as iron is lost by  
418 evaporation (Figure 7).

419 For experiments conducted at  $f\text{O}_2 = \text{IW-1}$ , on average 5% of the Fe starting material was  
420 lost to the Re wire (average  $X_{\text{Fe}}^{\text{wire}} = 0.05$ ), while this value is negligible at IW+2 (Figure 6b).  
421 Additionally, 13% of the Fe starting material was lost via evaporation at IW-1 (average  $X_{\text{Fe}}^{\text{gas}} =$   
422 0.13) and 8% of the starting material Fe was lost by evaporation at IW+2 (average  $X_{\text{Fe}}^{\text{gas}} = 0.08$ ).  
423 In one-atmosphere gas-mixing furnace experiments, Fe loss has generally been considered as loss  
424 to the container (e.g., Re or Pt wire), while volatile element loss (e.g., Na, K) has been attributed  
425 to vaporization (Corrigan and Gibb, 1979; Donaldson and Gibb, 1979; Grove, 1981; Borisov and  
426 Jones, 1999). Our results indicate that at IW-1, ~75% of the estimated Fe loss occurred via  
427 evaporation, and only 25% of the Fe loss can be attributed through loss to the Re wire. At IW+2,  
428 the estimated Fe loss is due to ~95% evaporative loss and ~5% loss to the Re wire.

429 To further assess the potential for evaporative isotopic fractionation at our experimental  
430 run conditions, we have calculated the evaporative flux of Fe ( $J_{\text{Fe}}$ ) from the sample using the Hertz-  
431 Knudsen equation:

432

$$J_{Fe} = \frac{\alpha_{Fe} (P_{Fe}^v - P_{Fe}^a)}{\sqrt{2\pi M_{Fe} RT}}$$

433 (4)

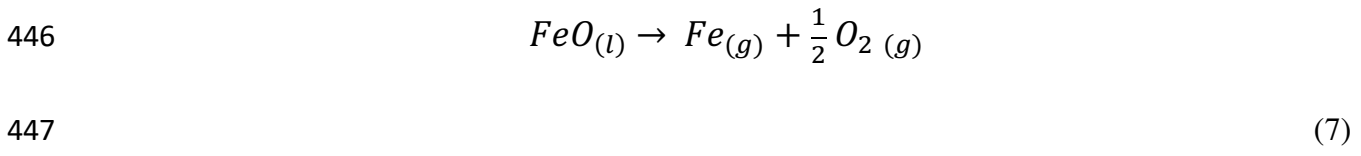
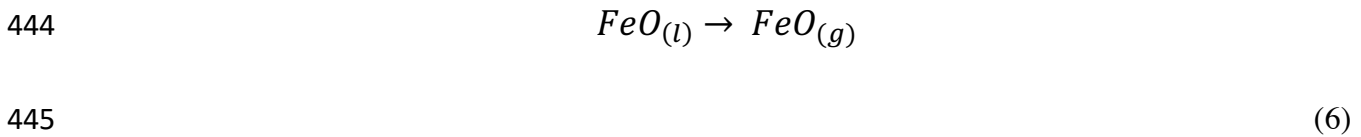
434 in which  $J$  is the evaporative flux in moles  $\text{cm}^{-2} \text{s}^{-1}$ ,  $\alpha$  is the evaporation coefficient,  $M$  is molecular  
 435 weight,  $P^v$  is equilibrium vapor pressure for the element considered,  $P^a$  is the ambient pressure for  
 436 the element considered,  $R$  is the universal gas constant ( $\text{J mol}^{-1} \text{K}^{-1}$ ), and  $T$  is temperature (K).  
 437 Following the methods outlined in Fedkin et al. (2006), we calculated the equilibrium vapor  
 438 pressure of Fe assuming both Fe and FeO species exist in the gas, and the only contribution of Fe  
 439 to the furnace gas atmosphere is from the experimental sample:

440

$$P_{Fe}^v = P_{Fe}^{sample} = P_{FeO} + P_{Fe}$$

441 (5)

442 The partial pressures of the gases evaporated from the molten experimental sample are then  
 443 calculated from the volatilization reactions:



448 The equilibrium constants,  $k$ , for reactions (6) and (7) are constructed from the thermodynamic  
 449 data in the JANAF tables (Chase, 1996) and used to calculate the equilibrium vapor pressure of  
 450 Fe:

451

$$P_{Fe}^{sample} = k_6 a_{FeO} + \frac{k_7 a_{FeO}}{\sqrt{f_{O_2}}}$$

452 (8)

453 where  $a_{FeO}$  is the activity of FeO in the molten experimental sample, and  $fO_2$  is the oxygen fugacity  
454 of the experiment. We used the rhyolite-MELTS code (Ghiorso and Sack, 1995; Asimow and  
455 Ghiorso, 1998; Gualda et al., 2012) to calculate the activity of FeO in the silicate liquid for each  
456 experimental starting composition at the experimental temperature and oxygen fugacity. Using  
457 equation (8), we calculate  $P_{Fe}^{sample}$ , which is then used to calculate the evaporative flux,  $J_{Fe}$ , from  
458 equation (4). Assuming the gas flow in our furnace is efficient in removing any Fe gas that is  
459 released into the furnace from the sample, we set the ambient vapor pressure of Fe ( $P^a$ ) equal to 0.  
460 Then, the only unknown needed to solve for the evaporative flux ( $J_{Fe}$ ) using equation (4) is the Fe  
461 evaporation coefficient ( $\alpha_{Fe}$ ). The evaporation coefficients we used in equation (4) to calculate  
462 evaporative Fe loss that matches the estimated evaporative Fe loss from our samples are  $\alpha_{Fe} =$   
463  $2.5 \times 10^{-3}$  at IW-1, and  $\alpha_{Fe} = 6.3 \times 10^{-2}$  at IW+2 (see Supplementary Material for additional detail).

464 Through isotopic measurement and mass balance calculations of our experiments, we have  
465 demonstrated that isotopic fractionation during evaporation and loss to the experimental container  
466 are essential considerations for experimental studies of isotope partitioning. Despite this open  
467 system behavior, the olivine and glass phases were always in equilibrium, as diffusion in the melt  
468 is fast (at 1265°C, anhydrous basaltic melt  $D_{Fe} \sim 10^{-11} \text{ m}^2/\text{s}$ ; Zhang et al., 2010), and 10-50  $\mu\text{m}$   
469 diameter olivine grains would diffusively equilibrate at the experimental run temperature and  
470 duration. For example, at experimental conditions of 1265°C and IW+2, a 50  $\mu\text{m}$  olivine grain  
471 would equilibrate with respect to Fe and Mg in approximately 50 hours (McDougall and Harrison,  
472 1999; Dohmen and Chakraborty, 2007). The olivine and glass separates showed deviation from  
473 the starting material, but had identical isotopic composition to that of the “total sample” which  
474 diffusively maintained equilibrium. Thus, the measured Fe isotopic compositions of the olivine

475 and glass can accurately be compared to interpret the olivine-melt Fe isotopic fractionation during  
476 olivine crystallization.

477

478 4.2. Factors controlling iron isotopic fractionation on the Moon

479 We have applied our results to test whether the lunar iron isotope “dichotomy” observed  
480 between the high- and low-Ti basalts can be explained by olivine crystallization or melt titanium  
481 content.

482 From our complementary NRIXS and olivine crystallization experiments, we have  
483 concluded that any equilibrium fractionation of iron isotopes between olivine and melt at lunar-  
484 like oxygen fugacities is not resolvable within analytical uncertainties. Olivine-melt Fe isotopic  
485 fractionation factors for the lunar volcanic glasses were determined from our measured force  
486 constants on the glass suite and the olivine NRIXS results from Dauphas et al. (2014) (Figure 8).  
487 Our result from the MC-ICPMS olivine crystallization study is consistent with the Fe isotopic  
488 fractionation factors predicted by the NRIXS measurements on olivine (Dauphas et al., 2014) and  
489 the suite of lunar volcanic glasses (this study), in that there is not a resolvable iron isotopic  
490 fractionation. Some major element variations in lunar mare basalts can be attributed to differences  
491 in source compositions having experienced varying degrees of olivine fractionation (Shearer et al.,  
492 2006, and references therein). Additionally, extensive crystallization of the lunar magma ocean  
493 involving significant fractionation of olivine has been previously hypothesized as a mechanism for  
494 generating the isotopically heavy source regions for the high-Ti basalts (Wang et al., 2015).  
495 However, because olivine does not fractionate iron isotopes to a measureable extent, varying  
496 degrees of equilibrium olivine crystallization can be eliminated as a potential mechanism for  
497 generating the mare basalt iron isotope dichotomy. The fractionation of phases other than olivine,

498 such as clinopyroxene and ilmenite, are likely more important in interpreting both the major  
499 element and isotopic compositions of the lunar mare basalt suites.

500 Both of our experimental approaches indicate that the difference in melt titanium content  
501 between low-Ti and high-Ti mare basalts cannot explain the observed iron isotope dichotomy.  
502 Partitioning of Fe into olivine has been shown to be a function of Ti content (Longhi et al., 1978;  
503 Xirouchakis et al., 2001; Krawczynski and Grove, 2012). Titanium influences the coordination  
504 environment of  $\text{Fe}^{2+}$  in silicate melt by forming Fe-Ti complexes, and as a result, Fe is  
505 preferentially incorporated into the melt relative to olivine (Krawczynski and Grove, 2012).  
506 However Fe isotope partitioning does not appear to correlate with melt titanium content, as  
507 demonstrated by our NRIXS force constant measurements (Table 4, Figure 4) and our olivine  
508 crystallization experiments from both the low-Ti and high-Ti glass compositions. Despite the  
509 different coordination of  $\text{Fe}^{2+}$  for different Ti contents. Though the major element partitioning of  
510 Fe into olivine is affected by  $\text{Fe}^{2+}$ -Ti complexes in silicate melt, the isotopic partitioning of Fe is  
511 not affected by melt titanium content. We conclude that  $\text{Fe}^{2+}$  coordination in silicate melts has a  
512 minimal effect on iron isotopic fractionation. In contrast, Dauphas et al. (2014) demonstrated that  
513 melt compositional parameters such as silica content and the redox state of iron (i.e.,  $\text{Fe}^{3+}$  content)  
514 influence the Fe bonding structure, and consequently, the iron isotopic composition, in a suite of  
515 terrestrial volcanic glass compositions ranging from basalt to rhyolite.

516

517 4.3. Iron isotopic composition of lunar dunite 72415

518 Olivines from lunar dunite 72415 are considerably lighter than the mare basalts ( $\delta^{56}\text{Fe}_{\text{dunite}}$   
519  $= -0.35 \pm 0.20\text{\textperthousand}$ , Wang et al., 2015; Sossi and Moynier, 2017). These values, if representative of  
520 equilibrium fractionation from a parent melt isotopically similar to the mare basalts ( $\delta^{56}\text{Fe} = 0\text{\textperthousand}$

521 to +0.2‰), differ from the predicted Fe isotopic fractionation of this study. The absence of  
522 resolvable equilibrium iron isotopic fractionation between olivine and lunar melts in our  
523 experiments supports a non-equilibrium model for generating the light iron isotopic composition  
524 of the lunar dunite.

525 As Fe begins to diffuse into olivine, the isotopes of Fe with lighter mass will be  
526 preferentially enriched, creating a “light” iron isotopic composition (Teng et al., 2008; Dauphas et  
527 al., 2010; Teng et al., 2011; Sio et al., 2013; Sio and Dauphas, 2017). The lunar dunite is highly  
528 magnesian (Fo<sub>84</sub> – Fo<sub>89</sub>, Dymek et al., 1975), and any Fe that diffuses into the olivine will greatly  
529 affect the mass balance of Fe isotopes in the dunite. Diffusive iron isotopic fractionation modeling  
530 that reproduces the observed Fe-Mg zoning profiles in lunar dunite olivine grains, can produce  
531 iron isotope signatures as low as  $\delta^{56}\text{Fe} = -0.21\text{\textperthousand}$  and -0.3‰ (Wang et al. 2015). Further, kinetic  
532 isotopic fractionation models of Fe-Mg interdiffusion and olivine crystallization (Teng et al., 2008;  
533 Teng et al., 2011; Sio et al., 2013; Oeser et al., 2015; Collinet et al., 2017; Sio and Dauphas, 2017)  
534 reproduce isotopic fractionations as large as 1‰ observed in olivine grains.

535 Models of lunar dunite (72415-72418) petrogenesis detail the potential petrologic  
536 processes involved in generating a kinetic origin for the isotopically light dunite signature. Early  
537 petrologic investigations of the lunar dunite identified it as an early lunar magma ocean cumulate  
538 (e.g., Dymek et al., 1975). In contrast, Ryder (1992) concluded that the lunar dunite crystallized at  
539 shallow depths less than 1 km. The early lunar magma ocean cumulate hypothesis was invoked by  
540 Wang et al. (2015) to explain the isotopically light iron isotopic compositions of the dunite. If the  
541 lunar dunite is an early lunar magma ocean cumulate, then, assuming equilibrium conditions, the  
542 composition from which the dunite is crystallizing must already be isotopically light;  $\delta^{56}\text{Fe} = -0.35$   
543  $\pm 0.20\text{\textperthousand}$ .

544 One way an isotopically light dunite source composition could potentially be generated is  
545 by an early core formation and metal-silicate partitioning. Experimental and analytical studies of  
546 metal-silicate iron isotope partitioning have suggested that metal is isotopically heavier ( $\Delta^{56}\text{Fe}_{\text{metal-}}$   
547  $\text{silicate} \approx +0.1\text{\textperthousand}$ ) than coexisting silicate (Poitrasson et al., 2005; Shahar et al., 2015; Elardo and  
548 Shahar, 2017). However, a number of investigations (e.g., Schuessler et al., 2007; Poitrasson et  
549 al., 2009; Hin et al., 2012; Shahar et al., 2016; Liu et al., 2017) have concluded that no significant  
550 iron isotopic fractionation occurs between metal and silicate in equilibrium. The disagreement  
551 results from the significant differences in starting compositions, phases, capsule materials, and  
552 experimental conditions between studies. Assuming an equilibrium iron isotopic fractionation did  
553 exist between metal and silicate, if the dunite source were once deep enough to be in isotopic  
554 equilibrium with the lunar core, it would have a relatively light iron isotopic composition.  
555 However, the estimates for the bulk mantle iron isotopic composition of the Moon after core  
556 formation (e.g., minimum  $\delta^{56}\text{Fe} = -0.15\text{\textperthousand}$ ; Elardo and Shahar, 2017), still cannot explain the  
557 magnitude of light iron isotopic compositions measured in the lunar dunite by equilibrium metal-  
558 silicate fractionation alone.

559 Another alternative method of generating isotopically light olivine in the lunar dunite is  
560 partial melting. Iron isotope studies of terrestrial peridotites, which are the residues of partial  
561 melting and depletion, show a correlation between iron isotopic compositions and depletion,  
562 becoming lighter at higher extents of partial melting (Williams et al., 2005; Weyer and Ionov,  
563 2007; Williams et al., 2009; Williams and Bizimis, 2014). It is possible that the iron isotopic  
564 composition of the lunar dunite is a result of partial melting, however the existing models of lunar  
565 dunite petrogenesis (i.e., Dymek et al., 1975; Ryder, 1992; Shearer et al., 2015) identify the dunite  
566 as being of cumulate origin, not an ultra-depleted residue of partial melting.

567 Considering the potential models for lunar dunite petrogenesis, kinetic fractionation via  
568 Fe-Mg interdiffusion seems likely to have occurred, and this mechanism could easily explain the  
569 light Fe isotopic compositions measured in the lunar dunite olivines. Regardless of whether the  
570 lunar dunite is a deep magma ocean cumulate (Dymek et al., 1975) or shallow cumulate (Ryder,  
571 1992; Shearer et al., 2015), the Mg-rich nature of the dunite ensures it would have interacted with  
572 a higher Fe/Mg melt before and/or during its ascent to the lunar surface/sub-surface. In this way,  
573 iron diffusion into the dunite is a plausible occurrence during every proposed model of dunite  
574 formation. Iron diffusion into the Fe-poor olivine of the lunar dunite would decrease the  $\delta^{56}\text{Fe}$   
575 composition, producing the negative  $\delta^{56}\text{Fe}$  values measured by both Wang et al. (2015) and Sossi  
576 and Moynier (2017).

577

#### 578 4.4 Considerations for High-Temperature Iron Isotopic Fractionation on Earth and Mars

579 The results of our olivine crystallization experiments indicate that the absence of a  
580 measureable equilibrium iron isotopic fractionation between olivine and melt is robust over  $f\text{O}_2$  =  
581 IW-1 to IW+2 in both the low-Ti (green glass) and high-Ti (black glass) compositions. Thus, we  
582 can apply our results for the synthetic lunar glass compositions to olivine-bearing systems on Earth  
583 and Mars with a similar range in oxygen fugacity, keeping in mind that there could be melt  
584 compositional controls in addition to that of  $\text{TiO}_2$  determined in this work.

585 Estimations for the oxygen fugacity of Earth's upper mantle from spinel peridotites lie  
586 within QFM±2 (IW+1.5 to IW+5.5 at magmatic temperatures), with select abyssal peridotites and  
587 peridotite massifs extending to QFM-3 (~IW+0.5) (Frost and McCammon, 2008, and references  
588 therein). Garnet peridotites are more reducing than spinel peridotites, with the majority of  $f\text{O}_2$   
589 estimations falling between IW-1 and IW+2 (Frost and McCammon, 2008). Additionally, the

590 oxygen fugacity of martian basalts is estimated to be QFM-3 to QFM-1 (~IW to IW+3) (Herd et  
591 al., 2002). Considering these estimates of magmatic oxygen fugacity, the IW-1 to IW+2 range of  
592 our experiments is relevant to garnet peridotites, as well as the most reduced spinel peridotites and  
593 martian basalts.

594 Iron isotopic compositions of terrestrial peridotites are  $\delta^{56}\text{Fe} = -0.1\text{\textperthousand}$  to  $+0.15\text{\textperthousand}$  (Dauphas et  
595 al., 2017). The range of peridotite iron isotopic compositions are considered to be a result of melt  
596 extraction based on the correlation between iron isotopic composition and depletion, with iron  
597 isotopic compositions of residues becoming lighter at higher extents of partial melting (Williams  
598 et al., 2005; Weyer and Ionov, 2007; Williams et al., 2009; Williams and Bizimis, 2014).  
599 Alternatively, the heavy isotopic enrichment in the melt relative to the residue may be a result of  
600  $\text{Fe}^{3+}$  in the melt (Dauphas et al., 2009a; Dauphas et al., 2014). For instance, the difference between  
601 the iron isotopic compositions of spinel and garnet peridotites has been attributed to the contrasting  
602 behavior of  $\text{Fe}^{3+}$  during melting (Williams et al., 2005). Experimental determinations of mineral-  
603 melt iron isotopic fractionations for additional minerals (i.e., pyroxene, spinel) are needed in order  
604 to fully model the evolution of iron isotopic compositions during partial melting, as there exists  
605 experimental evidence for equilibrium iron isotopic fractionation between spinel and olivine  
606 (Shahar et al., 2008; Roskosz et al., 2015).

607

## 608 5. Conclusion

609 Olivine separates are often enriched in lighter iron isotopes relative to coexisting minerals and  
610 the bulk rock (e.g., terrestrial peridotites, Beard and Johnson (2004); Poitrasson et al. (2004);  
611 Williams et al. (2005); terrestrial basalts, Teng et al. (2008); Teng et al. (2010); Sio et al. (2013);  
612 lunar basalts, Poitrasson et al. (2004); Wang et al. (2012); Wang et al. (2015); martian basalts,

613 Collinet et al. (2017)). Considering the olivine-melt fractionation results presented in this work,  
614 the only known mechanism capable of fractionating iron isotopes to a measureable degree is  
615 diffusive fractionation (Dauphas et al., 2010; Teng et al., 2011; Sio et al., 2013; Oeser et al., 2015;  
616 Sio and Dauphas, 2016; Collinet et al., 2017). Thus, the olivine grains enriched in light Fe isotopes  
617 in mafic rocks are not a result of primary igneous crystallization, but rather a diffusive  
618 fractionation, potentially related to re-equilibration (Teng et al., 2011; Sio et al., 2013; Oeser et  
619 al., 2015) or simultaneous Fe diffusion and crystal growth (Sio and Dauphas, 2016; Collinet et al.,  
620 2017). A diffusive fractionation mechanism is further supported by existing isotopic  
621 disequilibrium between coexisting mineral pairs in peridotite samples (Beard and Johnson, 2004;  
622 Roskosz et al., 2015). This disequilibrium in peridotites has been hypothesized as a result of  
623 multiple phases of melt extraction, melt percolation, melt-rock reaction, or metasomatism (Beard  
624 and Johnson, 2004; Williams et al., 2005; Macris et al., 2015; Roskosz et al., 2015; Zhao et al.,  
625 2017). If the light iron isotopic compositions of terrestrial peridotites can conclusively be attributed  
626 to metasomatism, then the light iron isotopic composition of the lunar dunite (discussed in Section  
627 4.3) may also be a result of metasomatism, as metasomatism has been invoked to explain chemical  
628 trends and petrographic textures observed in the lunar dunite (Shearer et al., 2015).

629

630

631 Acknowledgements

632 This work was supported by NASA grant NNX15AJ25G to MJK and ND, the McDonnell  
633 Center for the Space Sciences Roger B. Chaffee fellowship to KBP, and NSF (CSEDI  
634 EAR1502591 and Petrology and Geochemistry grant EAR1444951) and NASA (LARS  
635 NNX17AE86G, EW NNX17AE87G) grants to ND. The authors would like to thank Paul

636 Carpenter for his assistance with electron microprobe analyses, Prof. Robert Dymek for helpful  
637 discussions concerning the petrology of lunar dunite 72415-72418. Additionally, the authors thank  
638 Drs. Helen Williams, Catherine Macris, and Yongsheng He for providing thoughtful, constructive  
639 reviews of this manuscript, as well as Dr. Shichun Huang for additional comments and editorial  
640 handling.

641

642 Figure Captions

643 Figure 1. Iron isotopic compositions plotted as a function of  $\text{TiO}_2$ . Red points represent terrestrial  
644 basalts and andesites, and blue points represent lunar basalts. The terrestrial suite is similar in Fe  
645 isotopic composition to the low-Ti basalts, however high-Ti basalts have greater  $\delta^{56}\text{Fe}$  values. The  
646 observed fractionation between low- and high-Ti lunar mare basalts appears to be bi-modal,  
647 although it is uncertain if this modality is due to sampling bias, as basalts with intermediate Ti  
648 concentrations have not been frequently measured. Compositions and isotope measurement errors  
649 (95% confidence interval) are from (Wiesli et al., 2003; Poitrasson et al., 2004; Weyer et al., 2005;  
650 Teng et al., 2008; Dauphas et al., 2009b; Schuessler et al., 2009; Craddock et al., 2010; Liu et al.,  
651 2010; Wang et al., 2015; Sossi and Moynier, 2017).

652

653 Figure 2. Back scattered electron image of two olivine crystallization experiments. Both  
654 experiments were conducted at  $f\text{O}_2 = \text{IW}+2$ . Experiment durations were 1 day (left) and 4 days  
655 (right). Experimental olivine crystals (dark gray) in the 4-day experiment ( $\sim 50 \mu\text{m}$  diameter) are  
656 larger than those grown in the 1-day experiment ( $\sim 20 \mu\text{m}$ ). Additionally, the olivine grains are  
657 compositionally homogenous, i.e., there is no visible Fe zoning within the grains at the  $\pm 0.5$  wt.%  
658 FeO level.

659

660 Figure 3. a) Back scattered electron image of two Re wires. The wires were mounted in epoxy  
661 post-experiment and polished to create a measureable cross section. Both wires were used in  
662 experiments conducted at  $f\text{O}_2 = \text{IW}-1$ . Experiment durations were 6 hours (left) and 4 days (right).  
663 Experimental Fe loss to the Re wire increases with time, producing a thicker Fe-enriched layer  
664 (dark gray) while the core of the Re wire remains Fe-free (light gray).

665 b) Electron microprobe core-to-rim Fe (wt.%) profile in a Re wire from a 4-day experiment  
666 conducted at  $f\text{O}_2 = \text{IW-1}$ .

667

668 Figure 4. Force constants from a suite of melt compositions plotted as a function of  $\text{TiO}_2$  content.  
669 Red points represent the reduced ( $f\text{O}_2 = \text{IW}$ ) terrestrial basalt, andesite, and dacite glasses from  
670 Dauphas et al. (2014), and blue points represent the synthetic lunar volcanic glass compositions  
671 measured in this work. There is no correlation between force constants and  $\text{TiO}_2$  content within  
672 the investigated 0.4 - 16.3 wt.%  $\text{TiO}_2$  compositional range.

673

674 Figure 5. Iron isotopic compositions for each experiment part from Table 5 reported as  $\Delta^{56}\text{Fe}_{\text{part} -}$   
675  $\text{total sample}$  ( $\delta^{56}\text{Fe}_{\text{part}} - \delta^{56}\text{Fe}_{\text{total sample}}$ ). Error bars represent 95% confidence interval. Green symbols  
676 indicate a synthetic green glass starting composition, and black symbols indicate a synthetic black  
677 glass starting composition. Olivine and glass pairs from a given experiment are highlighted.

678

679 Figure 6.

680 a) A schematic diagram illustrating the Fe mass and isotope distributions detailed in Section 4.1  
681 for experiment H056. The labeled percent values at each branch represent the percent of the initial  
682 Fe attributed to a given experiment reservoir. Measured iron isotopic compositions of each  
683 experiment reservoir are mass balanced to explain the effect of Fe loss on the iron isotopic  
684 composition of the total sample. Iron isotopic compositions and fractionations in italics indicate  
685 calculated (not measured) values. Percent initial Fe for olivine and glass separates is calculated  
686 using the olivine and glass proportions given in Table 2 (83% glass, 17% olivine for H056) and  
687 the calculated percent initial Fe for the total sample ( $X_{\text{Fe}}^{\text{total sample}} = 1 - X_{\text{Fe}}^{\text{loss}}$ ). A similar calculation

688 was performed for each experiment using the measured iron isotopic compositions for all the  
689 experiment reservoirs (starting material, olivine, glass, total sample, experiment wire).

690

691 b) A stacked bar graph indicating the  $X_{Fe}$  calculated for each Fe reservoir for each experiment. The  
692 bracketed labels below the experiment names indicate the oxygen fugacity of the experiment (IW-  
693 1 or IW+2). Additionally, the legend identifies which reservoirs constitute Fe loss (wire, gas) and  
694 “total sample” Fe (olivine, glass).

695

696 Figure 7. The iron isotopic evolution of an experimental sample as evaporative Fe loss proceeds  
697 through Rayleigh distillation, as calculated using  $\alpha_{\text{experiment-vapor}}$  for each experiment. The iron  
698 isotopic composition is reported as  $\Delta^{56}\text{Fe}_{\text{sample}^* - \text{starting material}}$  ( $\delta^{56}\text{Fe}_{\text{sample}^*} - \delta^{56}\text{Fe}_{\text{starting material}}$ ) using  
699  $\delta^{56}\text{Fe}_{\text{starting material}}$  from Table 5.  $\delta^{56}\text{Fe}_{\text{sample}^*}$  represents the iron isotopic composition of the “total  
700 sample” after accounting for the iron isotopic fractionation associated with Fe loss to the Re wire  
701 (Section 4.1, Figure 6). This correction was performed to isolate the effect of evaporation on the  
702 heavy iron isotopic enrichment that occurs during the experiment, however both losses (to wire,  
703 to vapor) would occur simultaneously throughout the experiment. Green symbols indicate a  
704 synthetic green glass starting composition, and black symbols indicate a synthetic black glass  
705 starting composition. The shape of the symbols reflects the  $fO_2$  of each experiment as indicated in  
706 the legend. Each modeled line is labeled with the corresponding  $\alpha_{\text{experiment-vapor}}$  used in the Rayleigh  
707 distillation equation.

708

709 Figure 8. Equilibrium mineral-melt fractionation of iron isotopes for olivine plotted as a function  
710 of temperature. The blue line represents the difference between the average beta factor calculated

711 from the NRIXS mean force constants for our synthetic lunar glasses and the beta factor for olivine  
712 ( $\text{Fo}_{82}$ ) from Dauphas et al. (2014). The blue shading represents the error associated with the  
713 calculated beta factors. The difference between the iron isotopic compositions of olivine and glass  
714 separates in each crystallization experiment (Table 5) are plotted with the associated measurement  
715 errors (95% confidence interval). Green symbols indicate a synthetic green glass starting  
716 composition, and black symbols indicate a synthetic black glass starting composition. The inset in  
717 the bottom right is the same data plotted in the main figure, with the x-axis expanded on the  
718 experiment run temperatures. There is no resolvable difference between olivine and the synthetic  
719 lunar glass suite under equilibrium conditions, as evidenced by our experimental results from both  
720 the NRIXS and ICPMS approaches.

721

- 722 References:
- 723 Asimow, P.D. and Ghiorso, M.S. (1998) Algorithmic Modifications Extending MELTS to  
724 Calculate Subsolidus Phase Relations. *American Mineralogist* 83, 1127-1131.
- 725 Beard, B.L. and Johnson, C.M. (2004) Inter-mineral Fe isotope variations in mantle-derived rocks  
726 and implications for the Fe geochemical cycle. *Geochimica et Cosmochimica Acta* 68, 4727-4743.
- 727 Borisov, A. and Jones, J.H. (1999) An evaluation of Re, as an alternative to Pt, for the 1 bar loop  
728 technique: An experimental study at 1400°C. *American Mineralogist* 84, 1528-1534.
- 729 Chase, M.W. (1996) NIST-JANAF Thermochemical Tables for the Bromine Oxides. *Journal of*  
730 *Physical and Chemical Reference Data* 25, 1069.
- 731 Collinet, M., Charlier, B., Namur, O., Oeser, M., Médard, E. and Weyer, S. (2017) Crystallization  
732 history of enriched shergottites from Fe and Mg isotope fractionation in olivine megacrysts.  
733 *Geochimica et Cosmochimica Acta* 207, 277-297.
- 734 Corrigan, G. and Gibb, F.G.F. (1979) The loss of Fe and Na from a basaltic melt during  
735 experiments using wire-loop method. *Mineralogical Magazine* 43, 121-126.
- 736 Craddock, P.R. and Dauphas, N. (2011) Iron Isotopic Compositions of Geologic Reference  
737 Materials and Chondrites. *Geostandards and Geoanalytical Research* 35, 101-123.
- 738 Craddock, P.R., Dauphas, N. and Clayton, R.N. (2010) Mineralogical control on iron isotopic  
739 fractionation during lunar differentiation and magmatism, 41st Lunar and Planetary Science  
740 Conference, Houston, TX, p. 1230.
- 741 Dauphas, N. (2007) Diffusion-driven kinetic isotope effect of Fe and Ni during formation of  
742 Widmanstätten pattern. *Meteoritics and Planetary Science*, 1597-1613.
- 743 Dauphas, N., Craddock, P.R., Asimow, P.D., Bennett, V.C., Nutman, A.P. and Ohnenstetter, D.  
744 (2009a) Iron isotopes may reveal the redox conditions of mantle melting from Archean to Present.  
745 *Earth and Planetary Science Letters* 288, 255-267.
- 746 Dauphas, N., Janney, P.E., Mandybaev, R.A., Wadhwa, M., Richter, F.M., Davis, A.M., van  
747 Zuilen, M., Hines, R. and Foley, C.N. (2004) Chromatographic separation and multicollection-  
748 ICPMS analysis of iron. Investigating mass-dependent and -independent isotope effects.  
749 *Analytical chemistry* 76, 5855-5863.
- 750 Dauphas, N., John, S.G. and Rouxel, O. (2017) Iron Isotope Systematics. *Reviews in Mineralogy*  
751 and Geochemistry

- 752 Dauphas, N., Poitrasson, F., Burkhardt, C., Kobayashi, H. and Kurosawa, K. (2015) Planetary and  
753 meteoritic Mg/Si and  $\delta^{30}\text{Si}$  variations inherited from solar nebular chemistry. *Earth and Planetary*  
754 *Science Letters*, 236-248.
- 755 Dauphas, N., Pourmand, A. and Teng, F.-Z. (2009b) Routine isotopic analysis of iron by HR-MC-  
756 ICPMS: how precise and how accurate? *Chemical Geology* 267, 175-184.
- 757 Dauphas, N., Roskosz, M., Alp, E.E., Golden, D.C., Sio, C.K., Tissot, F.L.H., Hu, M.Y., Zhao, J.,  
758 Gao, L. and Morris, R.V. (2012) A *general moment* NRIXS approach to the determination of  
759 equilibrium Fe isotopic fractionation factors: Application to goethite and jarosite. *Geochimica et*  
760 *Cosmochimica Acta* 94, 254-275.
- 761 Dauphas, N., Roskosz, M., Alp, E.E., Neuville, D.R., Hu, M.Y., Sio, C.K., Tissot, F.L.H., Zhao,  
762 J., Tissandier, L., Médard, E. and Cordier, C. (2014) Magma redox and structural controls on iron  
763 isotope variations in Earth's mantle and crust. *Earth and Planetary Science Letters* 398, 127-140.
- 764 Dauphas, N. and Rouxel, O. (2006) Mass spectrometry and natural variations of iron isotopes.  
765 *Mass spectrometry reviews* 25, 515-550.
- 766 Dauphas, N., Teng, F.Z. and Arndt, N.T. (2010) Magnesium and iron isotope in 2.7 Ga Alexo  
767 komatiites: mantle signatures, no evidence for Soret diffusion, and identification of diffusive  
768 transport in zoned olivine. *Geochimica et Cosmochimica Acta* 74, 3274-3291.
- 769 Day, J.M.D., Qiu, L., Ash, R.D., McDonough, W.F., Teng, F.-Z., Rudnick, R.L. and Taylor, L.A.  
770 (2016) Evidence for high-temperature fractionation of lithium isotopes during differentiation of  
771 the Moon. *Meteoritics and Planetary Science* 51, 1046-1062.
- 772 Delano, J.W. (1986) Pristine Lunar Glasses: Criteria, Data, and Implications. *Journal of*  
773 *Geophysical Research* 91, D201-D213.
- 774 Dohmen, R. and Chakraborty, S. (2007) Fe-Mg diffusion in olivine II: point defect chemistry,  
775 change of diffusion mechanisms and a model for calculation of diffusion coefficients in natural  
776 olivine. *Phys Chem Minerals* 34, 409-430.
- 777 Donaldson, C.H. and Gibb, F.G.F. (1979) Changes in sample composition during experiments  
778 using 'wire-loop' technique. *Mineralogical Magazine* 43, 115-119.
- 779 Donovan, J.J., Singer, J.W. and Armstrong, J.T. (2016) A new EPMA method for fast trace  
780 element analysis in simple matrices. *American Mineralogist* 101, 1839-1853.
- 781 Dymek, R.F., Albee, A.L. and Chodos, A.A. (1975) Comparative petrology of lunar cumulate  
782 rocks of possible primary origin: Dunite 72415, troctolite 76535, norite 78235, and anorthositic  
783 62237. *Proceedings of the Lunar Science Conference* 6th, 301-341.

- 784 Elardo, S.M. and Shahar, A. (2017) Non-chondritic iron isotope ratios in planetary mantles as a  
785 result of core formation. *Nature Geoscience* 10, 317-321.
- 786 Fedkin, A.V., Grossman, L. and Ghiorso, M.S. (2006) Vapor pressures and evaporation  
787 coefficients for melts of ferromagnesian chondrule-like compositions. *Geochimica et*  
788 *Cosmochimica Acta* 70, 206-223.
- 789 Frost, D.J. and McCammon, C.A. (2008) The Redox State of Earth's Mantle. *Annu. Rev. Earth*  
790 *Planet. Sci.* 36, 389-420.
- 791 Ghiorso, M.S. and Sack, R.O. (1995) Chemical Mass Transfer in Magmatic Processes. IV. A  
792 Revised and Internally Consistent Thermodynamic Model for the Interpolation and Extrapolation  
793 of Liquid-Solid Equilibria in Magmatic Systems at Elevated Temperatures and Pressures.  
794 *Contributions to Mineralogy and Petrology* 119, 197-212.
- 795 Grove, T.L. (1981) Use of FePt Alloys to Eliminate the Iron Loss Problem in 1 Atmosphere Gas  
796 Mixing Experiments: Theoretical and Practical Considerations. *Contributions to Mineralogy and*  
797 *Petrology* 78, 298-304.
- 798 Gualda, G.A.R., Ghiorso, M.S., Lemons, R.V. and Carley, T.L. (2012) Rhyolite-MELTS: A  
799 modified calibration of MELTS optimized for silica-rich, fluid-bearing magmatic systems. *Journal*  
800 *of Petrology* 53, 875-890.
- 801 Herd, C.D.K., Borg, L.E., Jones, J.H. and Papike, J.J. (2002) Oxygen fugacity and geochemical  
802 variations in the martian basalts: Implications for martian basalt petrogenesis and the oxidation  
803 state of the upper mantle of Mars. *Geochimica et Cosmochimica Acta* 66, 2025-2036.
- 804 Hin, R.C., Schmidt, M.W. and Bourdon, B. (2012) Experimental evidence for the absence of iron  
805 isotope fractionation between metal and silicate liquids at 1 GPa and 1250-1300 °C and its  
806 cosmochemical consequences. *Geochimica et Cosmochimica Acta* 93, 164-181.
- 807 Krawczynski, M.J. and Grove, T.L. (2012) Experimental investigation of the influence of oxygen  
808 fugacity on the source depths for high titanium lunar ultramafic magmas. *Geochimica et*  
809 *Cosmochimica Acta* 79, 1-19.
- 810 Krawczynski, M.J. and Olive, J.L. (2011) A new fitting algorithm for petrological mass-balance  
811 problems, AGU Fall Meeting Abstracts, p. 2613.
- 812 Liu, J., Dauphas, N., Roskosz, M., Hu, M.Y., Yang, H., Bi, W., Zhao, J., Alp, E.E., Hu, J.Y. and  
813 Lin, J.-F. (2017) Iron isotopic fractionation between silicate mantle and metallic core at high  
814 pressure. *Nature communications* 8, 14377.

- 815 Liu, Y., Spicuzza, M.J., Craddock, P.R., Day, J.M.D., Valley, J.W., Dauphas, N. and Taylor, L.A.  
816 (2010) Oxygen and iron isotope constraints on near-surface fractionation effects and the  
817 composition of lunar mare basalt source regions. *Geochimica et Cosmochimica Acta* 74, 6249-  
818 6262.
- 819 Longhi, J., Walker, D. and Hays, J.F. (1978) The distribution of Fe and Mg between olivine and  
820 lunar basaltic liquids. *Geochimica et Cosmochimica Acta* 42, 1545-1558.
- 821 Macris, C.A., Manning, C.E. and Young, E.D. (2015) Crystal chemical constraints on inter-  
822 mineral Fe isotope fractionation and implications for Fe isotope disequilibrium in San Carlos  
823 mantle xenoliths. *Geochimica et Cosmochimica Acta* 154, 168-185.
- 824 McDougall, I. and Harrison, T.M. (1999) *Geochronology and thermochronology by the 40Ar/39Ar*  
825 method, Second Edition ed. Oxford University Press, New York, NY.
- 826 Millet, M.A., Dauphas, N., Greber, N.D., Burton, K.W., Dale, C.W., Debret, B., Macpherson,  
827 C.G., Nowell, G.M. and Williams, H.M. (2016) Titanium stable isotope investigation of magmatic  
828 processes on the Earth and Moon. *Earth and Planetary Science Letters* 449, 197-205.
- 829 Mullen, J.G. (1961) Isotope effect in intermetallic diffusion. *Physical Review*, 1649-1658.
- 830 Oeser, M., Dohmen, R., Horn, I., Schuth, S. and Weyer, S. (2015) Processes and time scales of  
831 magmatic evolution as revealed by Fe-Mg chemical and isotopic zoning in natural olivines.  
832 *Geochimica et Cosmochimica Acta* 154, 130-150.
- 833 Poitrasson, F., Halliday, A.N., Lee, D.-C., Levasseur, S. and Teutsch, N. (2004) Iron isotope  
834 differences between Earth, Moon, Mars and Vesta as possible records of contrasted accretion  
835 mechanisms. *Earth and Planetary Science Letters* 223, 253-266.
- 836 Poitrasson, F., Levasseur, S. and Teutsch, N. (2005) Significance of iron isotope mineral  
837 fractionation in pallasites and iron meteorites for the core-mantle differentiation of terrestrial  
838 planets. *Earth and Planetary Science Letters* 234, 151-164.
- 839 Poitrasson, F., Roskosz, M. and Corgne, A. (2009) No iron isotope fractionation between molten  
840 alloys and silicate melt to 2000 degrees C and 7.7 GPa: Experimental evidence and implications  
841 for planetary differentiation and accretion. *Earth and Planetary Science Letters* 278, 376-385.
- 842 Polyakov, V.B., Clayton, R.N., Horita, J. and Mineev, S.D. (2007) Equilibrium iron isotope  
843 fractionation factors of minerals: Reevaluation from the data of nuclear inelastic resonant X-ray  
844 scattering and Mössbauer spectroscopy. *Geochimica et Cosmochimica Acta* 71, 3833-3846.
- 845 Richter, F.M. (2004) Timescales determining the degree of kinetic isotope fractionation by  
846 evaporation and condensation. *Geochimica et Cosmochimica Acta* 68, 4971-4992.

- 847 Richter, F.M., Dauphas, N. and Teng, F.-Z. (2009) Non-traditional fractionation of non-traditional  
848 isotopes: Evaporation, chemical diffusion and Soret diffusion. *Chemical Geology* 258, 92-103.
- 849 Richter, F.M., Davis, A.M., Ebel, D.S. and Hashimoto, A. (2002) Elemental and isotopic  
850 fractionation of Type B calcium-, aluminum-rich inclusions: experiments, theoretical  
851 considerations, and constraints on their thermal evolution. *Geochimica et Cosmochimica Acta* 66,  
852 521-540.
- 853 Richter, F.M., Janney, P.E., Mandybaev, R.A., Davis, A.M. and Wadhwa, M. (2007) Elemental  
854 and isotopic fractionation of Type B CAI-like liquids by evaporation. *Geochimica et*  
855 *Cosmochimica Acta* 71, 5544-5564.
- 856 Roskosz, M., Luais, B., Watson, H.C., Toplis, M.J., Alexander, C.M.O.D. and Mysen, B.O. (2006)  
857 Experimental quantification of the fractionation of Fe isotopes during metal segregation from a  
858 silicate melt. *Earth and Planetary Science Letters* 248, 851-867.
- 859 Roskosz, M., Sio, C.K.I., Dauphas, N., Wenli, B., Tissot, F.L.H., Hu, M.Y., Zhao, J. and Alp, E.E.  
860 (2015) Spinel-olivine-pyroxene equilibrium iron isotopic fractionation and applications to natural  
861 peridotites. *Geochimica et Cosmochimica Acta* 169, 184-199.
- 862 Ryder, G. (1992) Chemical Variation and Zoning of Olivine in Lunar Dunite 72415: Near-Surface  
863 Accumulation. *Proceedings of Lunar and Planetary Science* 22, 373-380.
- 864 Sato, M. (1973) Oxygen fugacity values of Apollo 12, 14, and 15 lunary samples and reduced state  
865 of lunar magmas. *Lunar and Planetary Science Conference Proceedings* 4, 1061-1079.
- 866 Schuessler, J.A., Schoenberg, R., Behrens, H. and von Blanckenburg, F. (2007) The experimental  
867 calibration of the iron isotope fractionation factor between pyrrhotite and peralkaline rhyolitic  
868 melt. *Geochimica et Cosmochimica Acta* 71, 417-433.
- 869 Schuessler, J.A., Schoenberg, R. and Sigmarsdóttir, O. (2009) Iron and lithium isotope systematics  
870 of the Hekla volcano, Iceland - Evidence for Fe isotope fractionation during magma differentiation.  
871 *Chemical Geology* 258, 78-91.
- 872 Sedaghatpour, F., Teng, F.-Z., Liu, Y., Sears, D.W. and Taylor, L.A. (2013) Magnesium isotopic  
873 composition of the Moon. *Geochimica et Cosmochimica Acta* 120, 1-16.
- 874 Shahar, A., Elardo, S.M. and Macris, C.A. (2017) Equilibrium Fractionation of Non-traditional  
875 Stable Isotopes: an Experimental Perspective. *Reviews in Mineralogy and Geochemistry* 82, 65-  
876 83.

- 877 Shahar, A., Hillgren, V.J., Horan, M.F., Mesa-Garcia, J., Kaufman, L.A. and Mock, T.D. (2015)  
878 Sulfur-controlled iron isotope fractionation experiments of core formation in planetary bodies.  
879 *Geochimica et Cosmochimica Acta* 150, 253-264.
- 880 Shahar, A., Schable, E.A., Caracas, R., Gleason, A.E., Reagan, M.M., Xiao, Y., Shu, J. and Mao,  
881 W. (2016) Pressure-dependent isotopic composition of iron alloys. *Science* (New York, N.Y.) 352,  
882 580-582.
- 883 Shahar, A., Young, E.D. and Manning, C.E. (2008) Equilibrium high-temperature Fe isotope  
884 fractionation between fayalite and magnetite: An experimental calibration. *Earth and Planetary  
885 Science Letters* 268, 330-338.
- 886 Shearer, C.K., Elardo, S.M., Petro, N.E., Borg, L.E. and McCubbin, F.M. (2015) Origin of the  
887 lunar highlands Mg-suite: An integrate petrology, geochemistry, chronology, and remote sensing  
888 perspective. *American Mineralogist* 100, 294-325.
- 889 Shearer, C.K., Hess, P.C., Wieczorek, M.A., Pritchard, M.E., Parmentier, E.M., Borg, L.E.,  
890 Longhi, J., Elkins-Tanton, L.T., Neal, C.R., Antonenko, I., Canup, R.M., Halliday, A.N., Grove,  
891 T.L., Hager, B.H., Lee, D.-C. and Wiechert, U. (2006) Thermal and Magmatic Evolution of the  
892 Moon. *Reviews in Mineralogy and Geochemistry* 60, 365-518.
- 893 Sio, C.K.I. and Dauphas, N. (2016) Thermal and crystallization histories of magmatic bodies by  
894 Monte Carlo inversion of Mg-Fe isotopic profiles in olivine. *Geology*.
- 895 Sio, C.K.I. and Dauphas, N. (2017) Thermal and crystallization histories of magmatic bodies by  
896 Monte Carlo inversion of Mg-Fe isotopic profiles in olivine. *Geology* 45, 67-70.
- 897 Sio, C.K.I., Dauphas, N., Teng, F.-Z., Chaussidon, M., Helz, R.T. and Roskosz, M. (2013)  
898 Discerning crystal growth from diffusion profiles in zoned olivine by *in situ* Mg-Fe isotopic  
899 analyses. *Geochimica et Cosmochimica Acta* 123, 302-321.
- 900 Sossi, P.A. and Moynier, F. (2017) Chemical and isotopic kinship of iron in the Earth and Moon  
901 deduced from the lunar Mg-Suite. *Earth and Planetary Science Letters* 471, 125-135.
- 902 Teng, F.-Z., Dauphas, N. and Helz, R.T. (2008) Iron Isotope Fractionation During Magmatic  
903 Differentiation in Kilauea Iki Lava Lake. *Science* (New York, N.Y.) 320, 1620-1622.
- 904 Teng, F.-Z., Dauphas, N., Helz, R.T., Gao, S. and Huang, S. (2011) Diffusion-driven magnesium  
905 and iron isotope fractionation in Hawaiian olivine. *Earth and Planetary Science Letters* 308, 317-  
906 324.
- 907 Teng, F.-Z., Dauphas, N. and Watkins, J.M. (2017) Non-Traditional Stable Isotopes.

- 908 Van Orman, J.A. and Krawczynski, M.J. (2015) Theoretical constraints on the isotope effect for  
909 diffusion in minerals. *Geochimica et Cosmochimica Acta* 164, 365-381.
- 910 Wang, K. and Jacobson, S.B. (2016) Potassium isotopic evidence for a high-energy giant impact  
911 origin of the Moon. *Nature* 538, 487-490.
- 912 Wang, K., Jacobson, S.B., Sedaghatpour, F., Chen, H. and Korotev, R.L. (2015) The earliest Lunar  
913 Magma Ocean differentiation recorded in Fe isotopes. *Earth and Planetary Science Letters* 430,  
914 202-208.
- 915 Wang, K., Moynier, F., Dauphas, N., Barrat, J.-A., Craddock, P.R. and Sio, C.K. (2012) Iron  
916 isotope fractionation in planetary crusts. *Geochimica et Cosmochimica Acta* 89, 31-45.
- 917 Weyer, S., Anbar, A.D., Brey, G.P., Münker, C., Mezger, K. and Woodland, A.B. (2005) Iron  
918 isotope fractionation during planetary differentiation. *Earth and Planetary Science Letters* 240,  
919 251-264.
- 920 Weyer, S. and Ionov, D.A. (2007) Partial melting and melt percolation: The message from Fe  
921 isotopes. *Earth and Planetary Science Letters* 259, 119-133.
- 922 Wiesli, R.A., Beard, B.L., Taylor, L.A. and Johnson, C.M. (2003) Space weathering processes on  
923 airless bodies: Fe isotope fractionation in the lunar regolith. *Earth and Planetary Science Letters*  
924 216, 457-465.
- 925 Williams, H.M. and Bizimis, M. (2014) Iron isotope tracing of mantle heterogeneity within the  
926 source regions of oceanic basalts. *Earth and Planetary Science Letters* 404, 396-407.
- 927 Williams, H.M., Nielsen, S.G., Renac, C., Griffin, W.L., O'Reilly, S.Y., McCammon, C.A.,  
928 Pearson, N., Viljoen, F., Alt, J.C. and Halliday, A.N. (2009) Fractionation of oxygen and iron  
929 isotopes by partial melting processes: Implications for the interpretation of stable isotopes  
930 signatures in mafic rocks. *Earth and Planetary Science Letters* 283, 156-166.
- 931 Williams, H.M., Peslier, A.H., McCammon, C.A., Halliday, A.N., Levasseur, S., Teutsch, N. and  
932 Burg, J.-P. (2005) Systematic iron isotope variations in mantle rocks and minerals: The effects of  
933 partial melting and oxygen fugacity. *Earth and Planetary Science Letters* 235, 435-452.
- 934 Xirouchakis, D., Hirschmann, M.M. and Simpson, J.A. (2001) The effect of titanium on the silica  
935 content and on mineral-liquid partitioning of mantle-equilibrated melts. *Geochimica et*  
936 *Cosmochimica Acta* 65, 2201-2217.
- 937 Zhang, Y., Ni, H. and Chen, Y. (2010) Diffusion in Silicate Melts. *Reviews in Mineralogy and*  
938 *Geochemistry* 72, 311-408.

939 Zhao, X., Zhang, Z., Huang, S., Liu, Y., Li, X. and Zhang, H. (2017) Coupled extremely light Ca  
940 and Fe isotopes in peridotites. *Geochimica et Cosmochimica Acta* 208, 368-380.  
941